INTERNATIONAL JOURNAL FOR NUMERICAL METHODS IN FLUIDS
Int. J. Numer. Meth. Fluids 2006; **50**:1405–1423
Published online 9 December 2005 in Wiley InterScience (www.interscience.wiley.com). DOI: 10.1002/fld.1109

Euler flow in a supersonic mixed-compression inlet

Manish Kumar Jain[‡,§] and Sanjay Mittal[*,†]

Department of Aerospace Engineering, Indian Institute of Technology Kanpur, Kanpur, UP 208 016, India

SUMMARY

Numerical simulation of a two-dimensional mixed compression supersonic inlet is carried out by solving unsteady compressible Euler equations via a stabilized finite element method. The geometry of the inlet is similar to the one used by Anderson and Wong for experimental investigation for Mach 3 flow. The computations are capable of simulating the start-up problems associated with the inlet. The critical back pressure for the successful operation of the inlet is computed. The effect of inlet back pressure on the total pressure recovery and the flow distortion level is analysed. Contrary to the popular belief, it is found that in addition to the throat to inlet capture area ratio, the ramp geometry close to the throat plays an important role in the start-up dynamics. It is demonstrated via simulations that, everything else being same, the geometries of ramp upstream of the throat that are associated with a curvature higher than a certain threshold, result in unstarting the intake. Copyright © 2005 John Wiley & Sons, Ltd.

KEY WORDS: supersonic flow; air intake; mixed compression; finite element; Euler equations; start-up

1. INTRODUCTION

A supersonic intake decelerates the air from supersonic inflow to low subsonic at the outflow. It must provide sufficient amount of air under all operating conditions without disrupting high-lift/low-drag aerodynamics of the airframe. Efficiency of air-breathing engines depends strongly on the inlet characteristics. For flight Mach number greater than 2.5, a mixed-compression supersonic inlet is often used. It is characterized by multiple reflected oblique shocks in the convergent portion and a terminal normal shock immediately downstream of the throat. A typical mixed compression inlet consists of two parts: supersonic diffuser just upstream of the throat and a subsonic diffuser that lies downstream of the throat section. Details regarding the design and operation of a mixed compression inlet can be found in Reference [1]. During the critical operation of the inlet, the normal shock sits right at the

*Correspondence to: Sanjay Mittal, Department of Aerospace Engineering, Indian Institute of Technology Kanpur, Kanpur, UP 208 016, India.
†E-mail: smittal@iitk.ac.in
‡E-mail: manishK.jain@ge.com
§Formerly, Project Associate.

Received 19 April 2005
Revised 24 August 2005
Accepted 6 September 2005

throat and any further increase in the back pressure causes the flow to become unstable. In the subcritical regime, the normal shock is pushed in the convergent part of the intake. In such a state, the normal shock can be expelled out and the intake can 'unstart'. The air intake is also associated with the 'buzz' instability in which the normal shock oscillates back and forth in the convergent portion leading to high unsteadiness in the flow. It is encountered during the subcritical mode of operation of the supersonic inlet. Details on this flow instability can be found in the paper by Dailey [2]. In the present work, the 'start' and 'unstart' of inlet is simulated. However, the simulation of the 'buzz' instability requires the inclusion of viscous effects and will be attempted in future work.

The two basic characteristics that greatly influence the performance of the inlet are the total pressure recovery and the flow distortion exiting the inlet and entering the engine compressor. For efficient operation, a supersonic intake must provide high total pressure recovery and low flow distortion index. Total pressure recovery (TPR) is defined as the ratio of the area-weighted total pressure at inlet exit (p_{t02}) and free stream total pressure (p_{01}), i.e. $\mathrm{TPR} = p_{t02}/p_{01}$. Another important parameter that quantifies the quality of flow supplied to the engine is the inlet distortion (ID). This index is related to the non-uniformity of the flow across the engine face. It is defined as the difference between the maximum and minimum total pressures divided by the area-weighted total pressure at the inlet exit, i.e. $\mathrm{ID} = (p_{02_{\max}} - p_{02_{\min}})/p_{t02}$. Here, $p_{02_{\max}}$ and $p_{02_{\min}}$ are the maximum and minimum total pressure at the inlet exit, respectively.

Anderson and Wong [3] studied a two-dimensional supersonic mixed compression inlet at a design Mach number 3.0. A total pressure recovery of 0.90 was obtained with 14% boundary-layer bleed based on the captured mass flow. Wasserbauer *et al.* [4] conducted an experimental investigation on a full-scale mixed compression inlet designed for the TF30-P-3 turbofan engine. Their measurements indicate an overall loss in the total pressure recovery of nearly 10%. About 70% of the losses occur upstream of the throat station while the remaining 30% in the downstream part. The losses in the subsonic diffuser can be attributed mainly to the viscous effects. Majority of the total pressure losses in the inlet are due to the presence of shocks.

Numerical computations on supersonic inlets have been carried out by several researchers. For example, Knight [5, 6] studied two- and three-dimensional supersonic diffuser flows in simple geometries. Reynolds-averaged Navier–Stokes equations along with a turbulence equation were solved. Liang and Chan [7, 8] carried out a fairly comprehensive study of a two-dimensional mixed compression inlet. They solved the unsteady, compressible Navier–Stokes equations in conjunction with the Baldwin–Lomax turbulence model. The geometry of the inlet they modelled is similar to the one experimentally studied by Anderson and Wong [3]. More recently, Gokhale and Venkat [9] also analysed supersonic inlets for ramjet and scramjet engines by using a explicit, finite difference MacCormack scheme.

The governing equations for the inviscid flow analysis are the compressible Euler equations in the conservation law form. In the present computation, governing equations are solved using a stabilized finite element formulation based on conservation variables. The streamline-upwind/Petrov–Galerkin (SUPG) stabilization method [10–12] is employed to stabilize the computations against spurious numerical oscillations due to advection dominated flows. A shock capturing term is added to the formulation to provide stability to the computations in the presence of discontinuities and large gradients in the flow [13–15]. The impermeable wall boundary condition for velocity is treated implicitly by rotating the flows

locally. The normal and tangential components of the momentum are kept track of, rather than the Cartesian components. The normal component of the momentum can then be set to zero as a Dirichlet boundary condition. Movement between the normal-tangential components frame and the Cartesian components frame is accomplished by using a local transformation rule, dependent on the geometry of the boundary. More details on this can be found in Reference [16].

2. THE GOVERNING EQUATIONS

Let $\Omega \subset \mathbb{R}^2$ and $(0,T)$ be the spatial and temporal domains, respectively, and let Γ denote the boundary of Ω. The spatial and temporal coordinates are denoted by $\mathbf{x}$ and t. The Euler equations governing the fluid flow, in conservation form, are

$$\frac{\partial \rho}{\partial t} + \nabla \cdot (\rho \mathbf{u}) = 0 \quad \text{on } \Omega \text{ for } (0,T) \tag{1}$$

$$\frac{\partial (\rho \mathbf{u})}{\partial t} + \nabla \cdot (\rho \mathbf{u}\mathbf{u}) + \nabla p = \mathbf{0} \quad \text{on } \Omega \text{ for } (0,T) \tag{2}$$

$$\frac{\partial (\rho e)}{\partial t} + \nabla \cdot (\rho e \mathbf{u}) + \nabla \cdot (p\mathbf{u}) = 0 \quad \text{on } \Omega \text{ for } (0,T) \tag{3}$$

Here $\rho, \mathbf{u}, p$ and e are the density, velocity, pressure and the total energy per unit mass, respectively. Assuming, the air to be an ideal gas, the equation of state is given as $p = (\gamma - 1)\rho i$, where γ is the ratio of specific heats and i is the internal energy per unit mass. It is related to the total energy per unit mass and velocity as $i = e - \frac{1}{2}\|\mathbf{u}\|^2$. The temperature, θ, is related to the internal energy as $\theta = (\gamma - 1)/Ri$, where R is the ideal gas constant. The compressible Euler equations (1), (2), and (3) can be written in the conservation variables

$$\frac{\partial \mathbf{U}}{\partial t} + \frac{\partial \mathbf{F}_i}{\partial x_i} = \mathbf{0} \quad \text{on } \Omega \text{ for } (0,T) \tag{4}$$

where $\mathbf{U} = (\rho, \rho u_1, \rho u_2, \rho e)$, is the vector of conservation variables, and $\mathbf{F}_i$ is, the Euler vector defined as

$$\mathbf{F}_i = \begin{pmatrix} u_i \rho \\ u_i \rho u_1 + \delta_{i1} p \\ u_i \rho u_2 + \delta_{i2} p \\ u_i (\rho e + p) \end{pmatrix} \tag{5}$$

Here u_i are the components of the velocity. In the quasi-linear form, Equation (4) is written as

$$\frac{\partial \mathbf{U}}{\partial t} + \mathbf{A}_i \frac{\partial \mathbf{U}}{\partial x_i} = \mathbf{0} \quad \text{on } \Omega \text{ for } (0,T) \tag{6}$$

where $\mathbf{A}_i = \partial \mathbf{F}_i / \partial \mathbf{U}$ is the Euler Jacobian Matrix. Corresponding to Equation (6), the following boundary and initial conditions are chosen

$$\mathbf{U} = \mathbf{g} \quad \text{on } \Gamma_g \text{ for } (0, T) \tag{7}$$

$$\mathbf{U}(\mathbf{x}, 0) = \mathbf{U_0} \quad \text{on } \Omega_0 \tag{8}$$

3. FINITE ELEMENT FORMULATION

Consider a finite element discretization of Ω into subdomains Ω^e, $e = 1, 2, \ldots, n_{\text{el}}$, where n_{el} is the number of elements. Based on this discretization, we define the finite element trial function space $\mathscr{S}^h$ and weighting function space $\mathscr{V}^h$. These function spaces are selected, by taking the Dirichlet boundary conditions into account, as subsets of $[\mathbf{H}^{1h}(\Omega)]^{n_{\text{dof}}}$, where $\mathbf{H}^{1h}(\Omega)$ is the finite-dimensional function space over Ω and n_{dof} is the number of degrees of freedom. The stabilized finite element formulation of Equation (6) is written as follows: find $\mathbf{U}^h \in \mathscr{S}^h$ such that $\forall \mathbf{W}^h \in \mathscr{V}^h$,

$$\int_\Omega \mathbf{W}^h \cdot \left(\frac{\partial \mathbf{U}^h}{\partial t} + \mathbf{A}_i^h \frac{\partial \mathbf{U}^h}{\partial x_i} \right) \mathrm{d}\Omega + \sum_{e=1}^{n_{\text{el}}} \int_{\Omega^e} \boldsymbol{\tau} (\mathbf{A}_k^h)^{\mathrm{T}} \left(\frac{\partial \mathbf{W}^h}{\partial x_k} \right) \cdot \left[\frac{\partial \mathbf{U}^h}{\partial t} + \mathbf{A}_i^h \frac{\partial \mathbf{U}^h}{\partial x_i} \right] \mathrm{d}\Omega$$
$$+ \sum_{e=1}^{n_{\text{el}}} \int_{\Omega^e} \delta \left(\frac{\partial \mathbf{W}^h}{\partial x_i} \right) \cdot \left(\frac{\partial \mathbf{U}^h}{\partial x_i} \right) \mathrm{d}\Omega = \mathbf{0} \tag{9}$$

In the variational formulation given by Equation (9), the first two terms and the right-hand side constitute the Galerkin formulation of the problem. The first series of element-level integrals in Equation (9) are the SUPG stabilization terms added to the variational formulation to stabilize the computations against node-to-node oscillations in the advection–dominated range. The SUPG formulation for the convection dominated flows was introduced by Hughes and Brooks [10] and Brooks and Hughes [11]. It was extended to the computation of compressible flows in the context of compressible Euler equations by Tezduyar and Hughes [12] and Hughes and Tezduyar [17].

SUPG is an excellent method for computing problems with relatively smooth solutions. However, it is not able to effectively control the localized oscillations that may arise due to sharp layers and discontinuities. Hughes *et al.* [18] introduced a discontinuity-capturing term that senses the sharp layers in the solution and acts only in the local region. In that sense, unlike the SUPG, it is a non-linear method even when it is applied to a linear advection–diffusion equation. The SUPG formulation along with the discontinuity-capturing term was recast in the entropy variables formulation can be found in the work by Hughes *et al.* [19]. It was shown in LeBeau and Tezduyar [13] that the accuracy of the SUPG formulation in conservation variables when supplemented with the discontinuity-capturing term, introduced originally for entropy variables formulation, gives comparable accuracy. The second series of element level integrals in the formulation given by Equation (9) are the shock capturing terms that stabilize the computations in the presence of sharp gradients [13]. The stabilization coefficients δ and $\boldsymbol{\tau}$ are the ones that were used in our earlier work [14, 20] and quite

similar to those employed by Aliabadi and Tezduyar [21]. They are defined as

$$\boldsymbol{\tau} = \max[\mathbf{0}, \boldsymbol{\tau}_a - \boldsymbol{\tau}_\delta] \tag{10}$$

$$\boldsymbol{\tau}_a = \frac{h}{2(c + \|\mathbf{u}\|)}\mathbf{I} \tag{11}$$

$$\boldsymbol{\tau}_\delta = \frac{\delta}{2(c + \|\mathbf{u}\|)^2}\mathbf{I} \tag{12}$$

$$\delta = \left[\frac{\left(\dfrac{\partial \mathbf{U}^h}{\partial t} + \mathbf{A}_i \dfrac{\partial \mathbf{U}^h}{\partial x_i}\right) \cdot \mathbf{A}_0^{-1} \left(\dfrac{\partial \mathbf{U}^h}{\partial t} + \mathbf{A}_j \dfrac{\partial \mathbf{U}^h}{\partial x_j}\right)}{\dfrac{\partial \zeta_l}{\partial x_j}\dfrac{\partial \mathbf{U}^h}{\partial x_j} \cdot \mathbf{A}_0^{-1} \dfrac{\partial \zeta_l}{\partial x_k}\dfrac{\partial \mathbf{U}^h}{\partial x_k}} \right]^{1/2} \tag{13}$$

where c is the wave speed, h is the element length, $\zeta_l, l = 1, 2$ are the components of the (element) local coordinates and $\mathbf{A}_0^{-1}$ is the inverse of Reimannian metric tensor related to the transformation between the conservation and entropy variables [22]. Compared to the definition for δ in Le Beau and Tezduyar [13] the definition given by Equation (13), introduced by Mittal [14, 20], includes the unsteady term in the computation of the residual for calculating the shock-capturing parameter. The inclusion of this term renders consistency to the formulation, even for unsteady computations, at-least in the case of inviscid flows. It was reported in Reference [14] that, if the unsteady term is not included in the definition of δ, one may obtain overly damped solutions for unsteady flow problems. For, e.g. in the computation of unsteady flow past a NACA0012 airfoil at $Re = 10\,000$ and zero incidence, the exclusion of the unsteady term in Equation (13) alters the vortex shedding, significantly. Of course, for steady computations, this term does not affect the final solution. In fact, one would like to drop this term to gain extra stability to converge to the final solution. In the present work, most of the computations lead to steady solutions. In such cases, the inclusion of the unsteady term in Equation (13) has no effect on the final solution. The matrix $\boldsymbol{\tau}_\delta$ is subtracted from $\boldsymbol{\tau}_a$ to account for the shock-capturing term as shown in Equation (10).

To facilitate the implementation of the boundary conditions for the velocity field for the Euler equations, the velocity at a solid boundary is written, not in terms of the Cartesian components, but the normal and tangential components. This rotation is applied at each node and a homogeneous Dirichlet boundary condition is applied to the normal component of velocity on each node lying on a solid surface. The details of the implementation can be found in Reference [16]. The extension of the formulation, presented above, to compute viscous flows and its applications to various internal and external flows can be found in our earlier articles [14, 15, 20, 23].

The time discretization of the variational formulation given by Equation (9) is done via the generalized trapezoidal rule. For unsteady computations, we employ a second-order accurate-in-time procedure.

4. RESULTS

4.1. Inlet geometry and computational domain

The two-dimensional supersonic flow mixed compression inlet that is studied here is similar to the one employed by Anderson and Wong [3] for their experimental investigations. The details of the inlet, along with the dimensions, are shown in Figure 1. The geometric throat is located at 58.8″ from the leading edge of the intake. The first compression ramp is at an angle of 7° to the flow and is 28″ long. It is followed by the second ramp which is at an angle of 14° to the free-stream flow. The geometry of the ramp surface between the end of second linear segment of the ramp and throat, i.e. points *d* and *e* (refer to Figure 1), is defined by a cubic polynomial. The four constants of this polynomial are evaluated based on the locations and slopes of points *d* and *e*. In the intake employed by Anderson and Wong [3], the second ramp extends to 54.1″ from the leading edge. This configuration will be referred to as *R*54.1 and is shown in Figure 2 along with other ramp geometries. The geometry shown in Figure 1, *R*52.1, extends to 52.1″ from the leading edge of the intake. In the present study, computations are carried out for four ramp geometries. These are shown in Figure 2. For two of them, the inlet fails to 'start'. Anderson and Wong [3] had performed experiments on the air intake with various lengths of the subsonic part of the diffuser. In the present work, the geometry with the short diffuser has been studied. The total length of the intake is 101.5″.

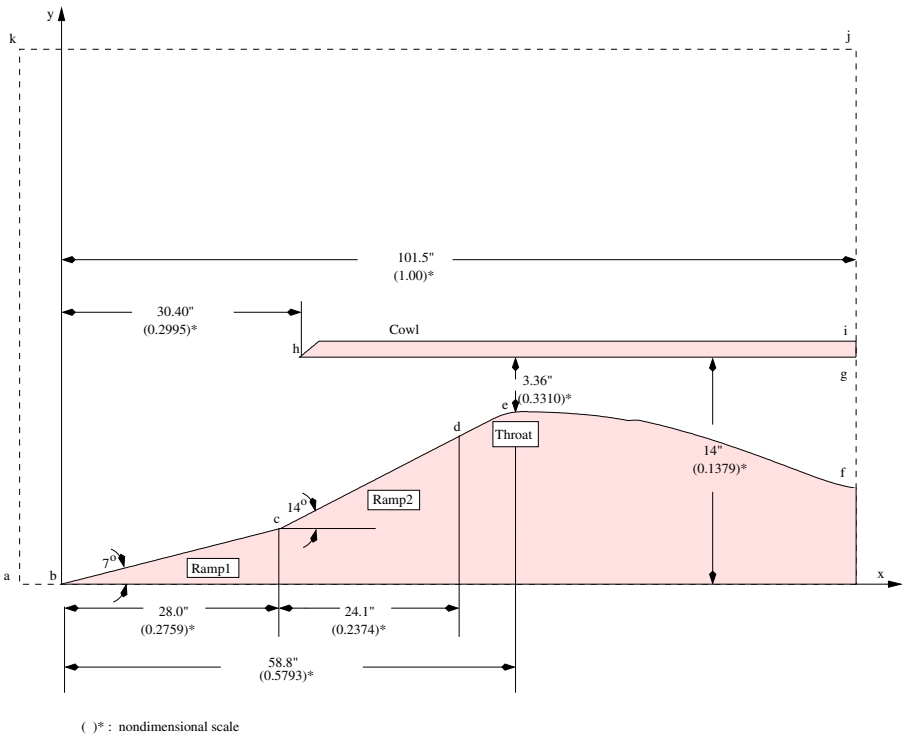

Figure 1. Geometry of the supersonic mixed-compression inlet.

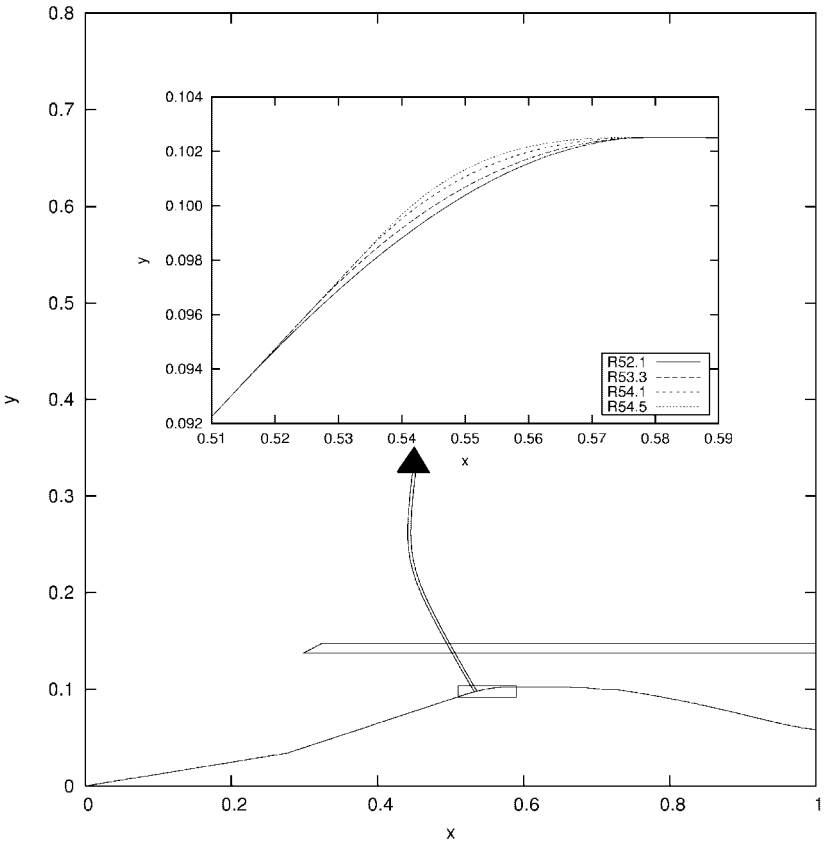

Figure 2. Geometries of the air intakes with different lengths of the second ramp. All intakes have the same total length and throat area.

The throat area for the present study is an increase of 7% over the original geometry that was used by Anderson and Wong [3]. In their experiments with the *R*54.1 geometry, Anderson and Wong [3] had employed a 14% boundary layer bleed based on the captured mass flow. In the present study, with no boundary layer effects being simulated, bleed is not being used. Consequently, the throat area of the original geometry is not enough to allow all the captured mass flow to pass through. A terminal normal shock appears upstream of the throat and is eventually expelled out. Hence, the inlet geometry is modified to operate with the increased mass flow rate (without bleed). Figure 1 shows the modified geometry that is being used in this study.

A schematic of the computational domain is also shown in Figure 1 via broken lines. The length of the intake, 101.5″, is utilized to non-dimensionalize the spatial dimensions. The flow enters through the boundary a–k and exits from the boundaries f–g and i–j. The non-dimensional height of the computational domain, a–k, is 0.98. The inflow boundary is located 0.2 units upstream of the leading edge of the inlet. The vertical location of boundary j–k is chosen such that the shock from the engine cowl, h–i, leaves the computational domain through the outflow boundary i–j. Internal as well as flow external to the intake is

computed. In contrast, the vertical extent of the computational domain for the study by Liang and Chan [8] is restricted to the height of the intake. All the results in the article are shown with respect to the non-dimensionalized variables.

4.2. Boundary and initial conditions

Figure 1 shows the extent of the computational domain via broken lines. Free-stream conditions corresponding to Mach 3 flow are specified at the inflow boundary $a-k$. The free-stream flow is aligned with the intake. On the cowl and the ramp surface, the normal component of the velocity is assigned a zero value. The tangential component of velocity is unknown and is determined from the computations. On the upper and lower boundaries, $a-b$ and $j-k$, the normal component of velocity is specified to be zero. The initial condition for the computations corresponds to the specification of free-stream conditions in the entire domain. At $t=0^+$ the boundary conditions on the intake and the cowl walls are enforced. First, computations are carried out for supersonic outflow at the exit $f-g$ of the intake. This is achieved by specifying no boundary conditions at the outflow. Once the flow is established and a steady-state flow has been realized, the back-pressure, p_b, at the exit of the intake is imposed. Computations are carried out for various values of p_b/p_i, where, p_i is the inlet static pressure. p_b/p_i is increased till at a certain critical value the inlet 'unstarts'.

4.3. The finite element mesh and convergence

The finite element mesh consists of a combination of structured and unstructured parts. Close to the solid boundaries, a structured mesh is generated. This will be useful for controlling the size of elements within the boundary layer when attempting viscous computations in future. The unstructured mesh is created using Delaunay triangulation. A typical mesh used for the computations is shown in Figure 3.

To establish the adequacy of the finite element mesh being used in this study, a convergence study has been carried out. The solution for the $R52.1$ geometry with $p_b/p_i=20$ is computed with three different meshes. Mesh $M1$ consists of 67 339 triangular elements and 34 182 nodes. In mesh $M2$ the number of elements and nodes are, 127 012 and 64 274, respectively. The corresponding numbers for mesh $M3$ are 214 528 and 108 288. The solutions obtained with the three meshes are shown in Figures 4 and 5. The maximum difference at any node between the results obtained with meshes $M1$ and $M2$ is less than 3%. The results obtained with meshes $M2$ and $M3$ are virtually identical. This suggests that mesh $M2$ is adequate to accurately capture all the details associated with this flow. All the results in the remaining part of the paper have been computed by using mesh $M2$.

The flow structure observed in Figure 4 is very typical of that seen in such air intakes. The oblique shock generated from the first ramp hits the cowl lip and is reflected back to the ramp. Another oblique shock is generated at the second ramp and subsequent reflections result in a train of shock waves. The flow is slowed down by each of the shock as shown in the plot showing the Mach number distribution in Figure 5. The rise in pressure after each shock can also be noticed in the plot showing the pressure distribution in Figure 5. As a result of the flow deceleration, the Mach number at the geometric throat is slightly higher than 1.0. In the divergent part, downstream of the throat, the flow expands. To adjust to the specified pressure at the exit, a normal shock is formed in the latter part of the intake. As the back pressure at the exit of the intake is increased, the normal shock moves upstream till

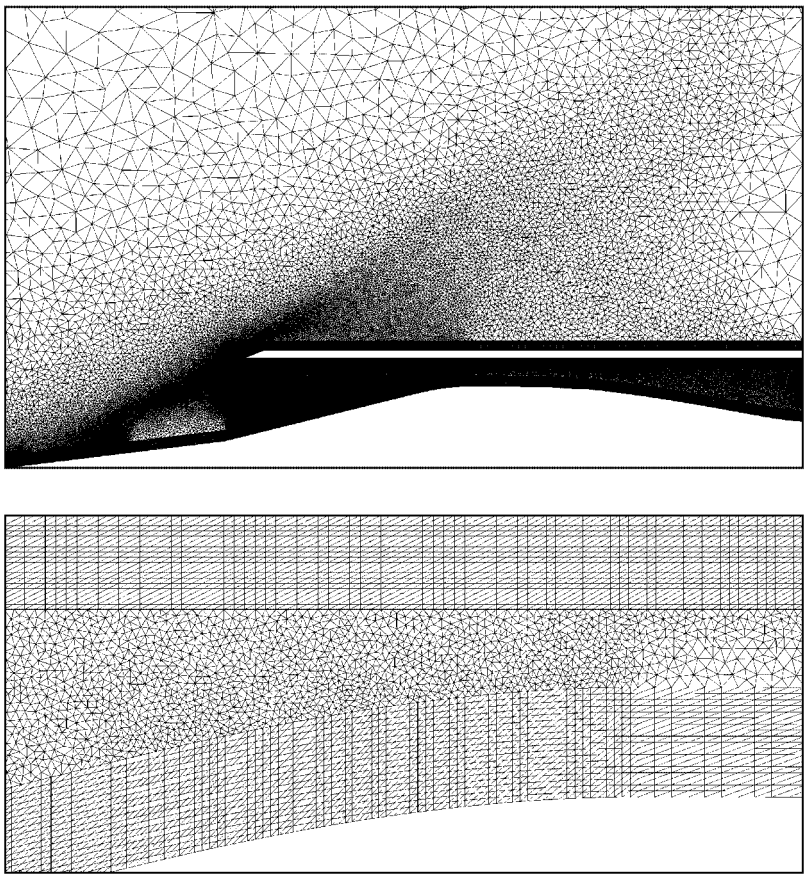

Figure 3. Flow in an air intake: close up views of the finite element mesh. The mesh consists of 64 274 nodes and 127 012 triangular elements. The lower figure shows the mesh in the throat region.

it reaches the throat. Any further increase in the back pressure results in the expulsion of the shock and the inlet 'unstarts'.

4.4. Effect of back pressure

Computations are carried out for various back pressure conditions at the exit of the air intake corresponding to the *R*52.1 configuration. Figure 6 shows the Mach number field for various values of the back pressure. The top row shows the solution for the case when no boundary condition is applied at the intake exit. This results in a supersonic flow at the outflow. On imposing back pressure, a normal shock appears in the divergent portion of the intake, and the flow at the exit becomes subsonic. The shock moves upstream towards the throat as the back pressure is increased. For $p_b/p_i = 32.4$, the normal shock reaches the geometric throat. The Mach number and pressure along the ramp surface for various values of back pressure are shown in Figure 7.

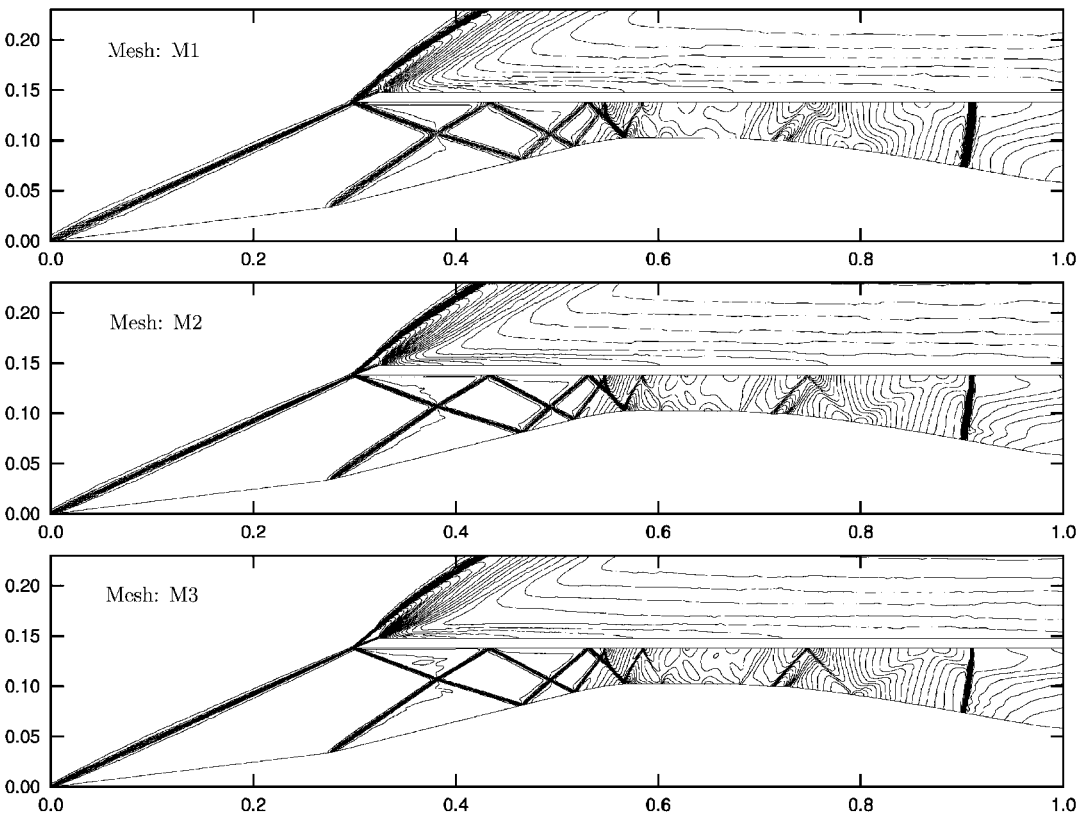

Figure 4. $M = 3$, $p_b/p_i = 20$ flow in an air intake: iso Mach number contours obtained with different finite element meshes.

Also shown in Figure 7 is the pressure distribution reported by Liang and Chan [8] for their computations for $p_b/p_i = 31$. The agreement between the present results and those from Liang and Chan [8] is excellent in the convergent part of the inlet. The results reported by Liang and Chan [8] are for a longer diffuser geometry corresponding to a total intake length of $119''$. Also, while Liang and Chan [8] computed a viscous flow, the present study is restricted to inviscid flow. To start the inlet they found it necessary to increase the throat area by 2%, as compared to the geometry used by Anderson and Wong [3] and use a minimum of 12% of boundary layer bleed. In addition, they simulated the effect of vortex generators in their computations. For these reasons, there are some differences between the pressure distributions from the two sets of computations downstream of the throat. The critical value of p_b/p_i from the present study is 32.4. It is close to 31.5 from the study by Liang and Chan [8]. As expected, viscous effects lower the critical back pressure for stable operation of the intake. Qualitatively, the two sets of results, close to the critical value of back pressure, are in good agreement.

An optimal inlet operating point requires the flow to have a high total pressure recovery and a low flow distortion level. To achieve this objective the terminal normal shock should be located close to the geometric throat. For $p_b/p_i = 32.4$, the total pressure recovery and flow distortion factor are found as 92.8 and 4%, respectively. Liang and Chan [8] found the

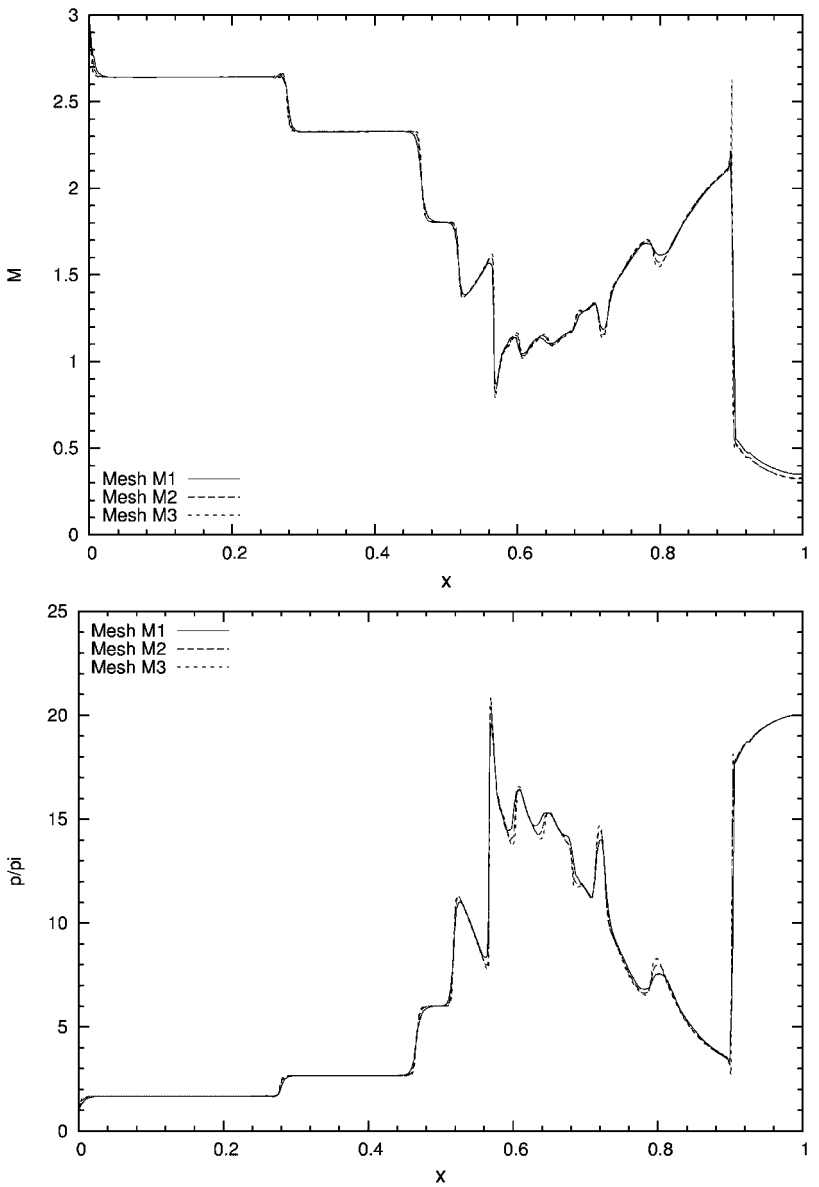

Figure 5. $M = 3$, $p_b/p_i = 20$ flow in an air intake: Mach number (top) and pressure (bottom) distribution on the ramp surface obtained with different finite element meshes.

corresponding total pressure recovery at the critical pressure ($= 31.5\, p_i$) to be 87.6%. For $p_b/p_i = 31.5$, the present computations result in pressure recovery of ~ 90.5. As expected, the numbers indicate that the viscous effects lead to a deterioration in the performance of the inlet. In the current study, based on the locations of geometric throat and normal shock, the inlet stability margin, at the critical pressure, is found to be 2.57%.

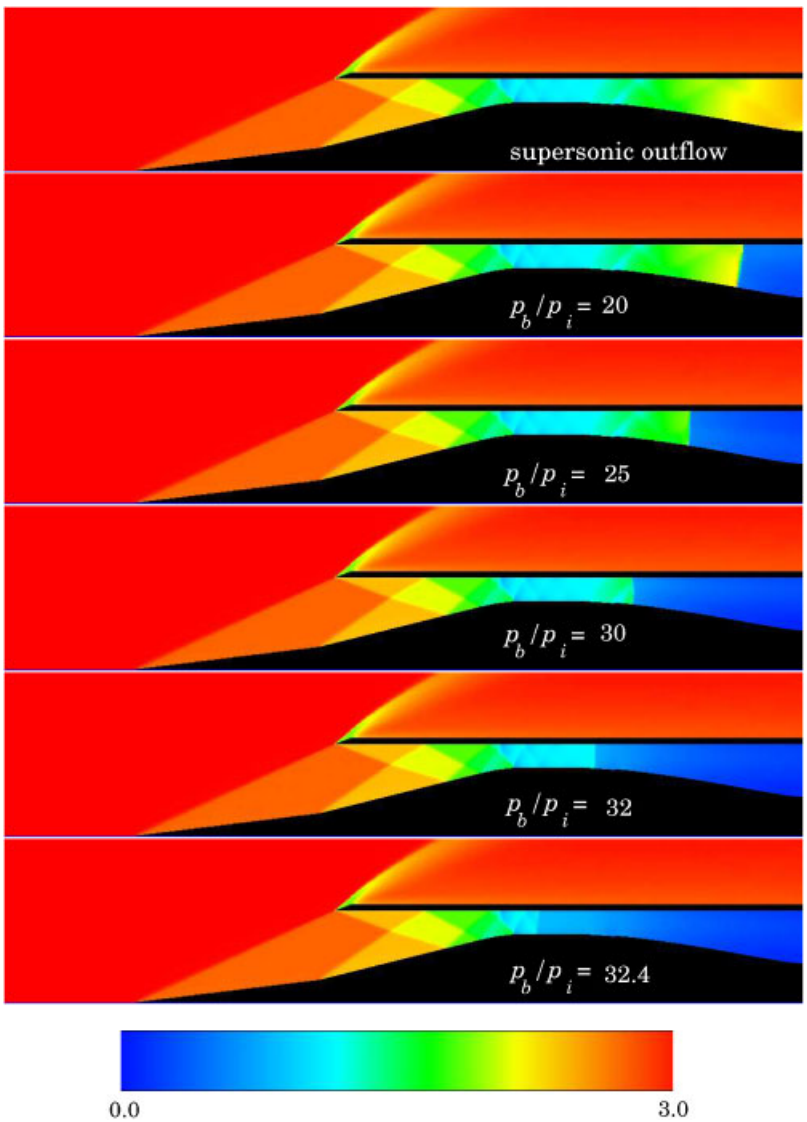

Figure 6. $M = 3$ flow in an air intake for the $R52.1$ ramp geometry: Mach number distribution for different values of back pressure. Also shown is the associated colour map.

On increasing p_b/p_i to 32.42 the normal shock moves to the convergent part, ahead of the throat, and the inlet unstarts. The Mach number distribution at various time instants is shown in Figure 8. It is interesting to notice the movement of the normal shock and its interaction with the other shocks as it is expelled out. The slip stream that is generated when a normal shock intersects an oblique shock is clearly observed in these pictures. As the normal shock moves upstream of the second ramp and the cowl-lip, the external flow over the cowl is also disturbed and its spillage is quite apparent. Eventually, the normal shock hits the upstream

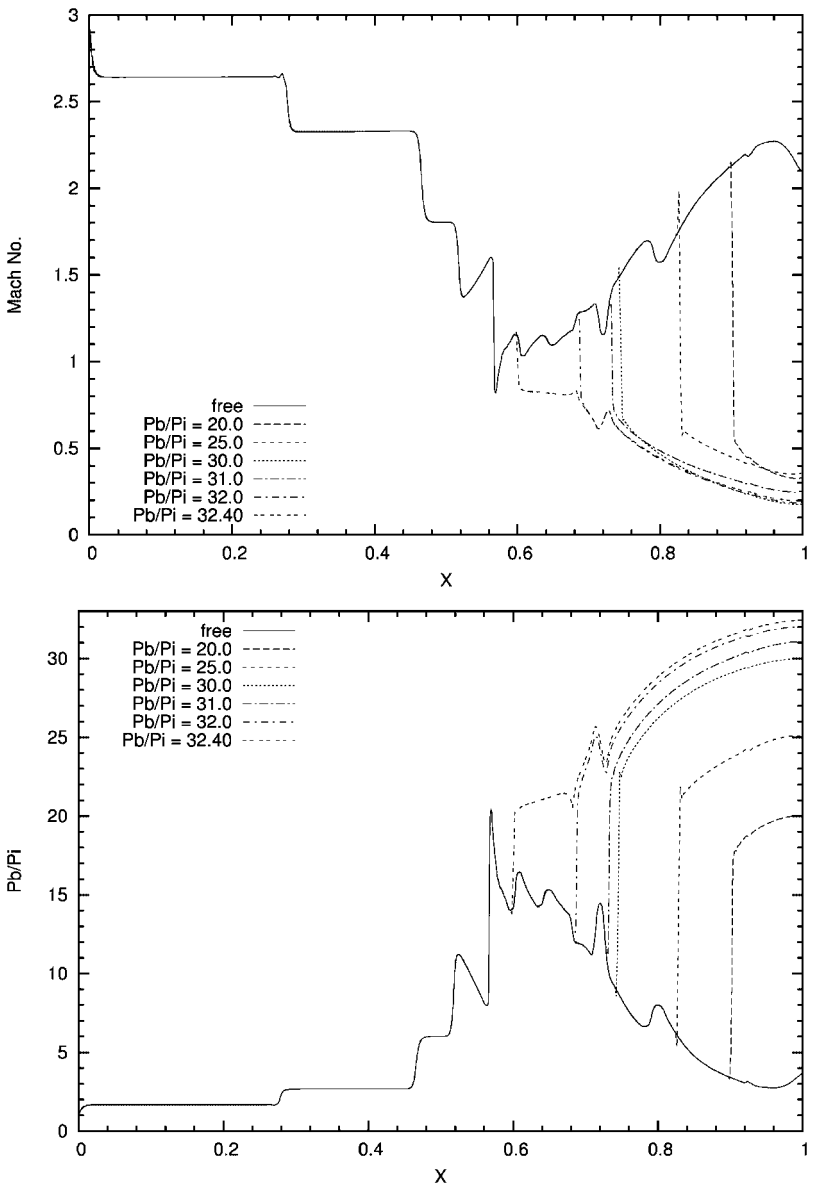

Figure 7. $M = 3$ flow in an air intake for the $R52.1$ ramp geometry: Mach number (top) and pressure on the ramp (bottom) distribution for different values of back pressure.

boundary at which point the computations break down. This simulation clearly demonstrates the capability of the present methodology to predict 'unstart' of air intakes. In the next step we would like to include the viscous effects and look into the possibility of simulating the 'buzz instability' [2] in air intakes.

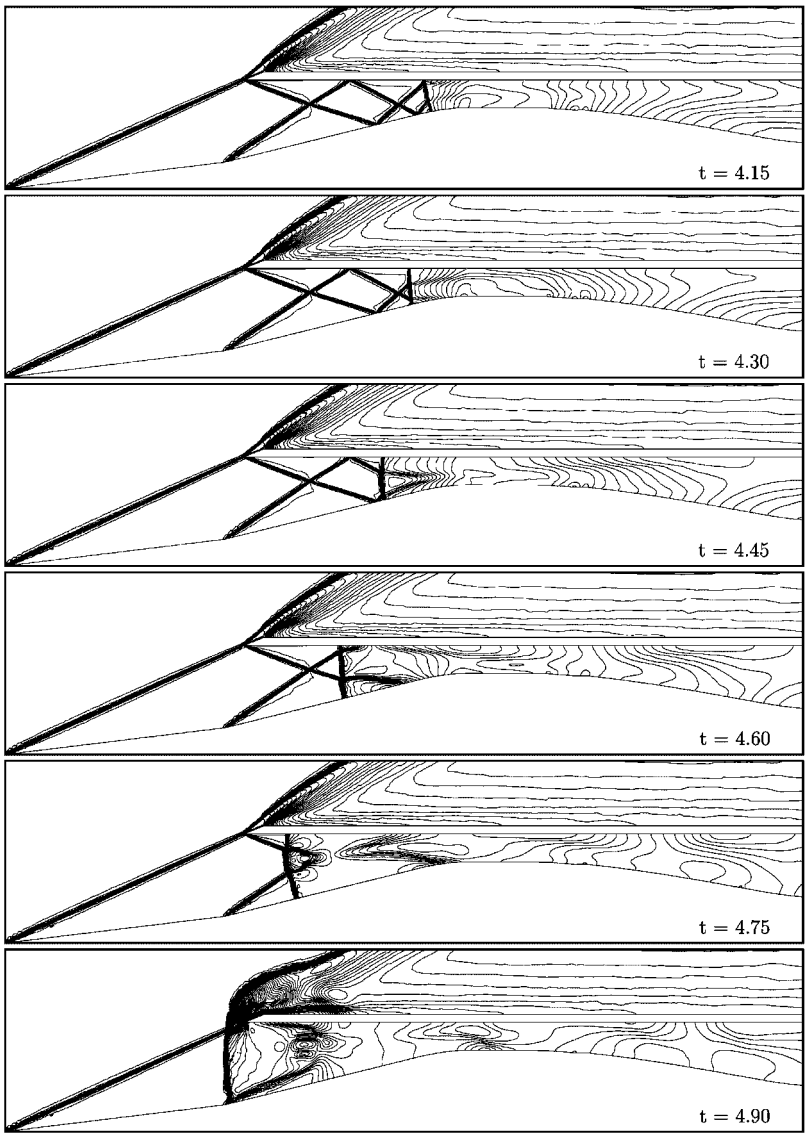

Figure 8. $M = 3$, $p_b/p_i = 32.42$ flow in an air intake for the $R52.1$ ramp geometry: Mach number distribution at various time instants.

TPR and ID for various values of the back pressure are shown in Figures 9 and 10. They are found in good agreement with the experimental data [3]. Also shown in Figure 9 is the contribution of the normal shock and oblique shocks to the total pressure loss. Using the Rankine–Hugoniot relations, the total pressure loss across a terminal normal shock at Mach 3.0 is found to be 67.17%. In contrast, the total pressure loss for the present intake for $p_b/p_i = 32.4$ is 7.18%. The present computations show that the TPR and ID are within acceptable limits for the intake to operate at $p_b/p_i \sim 32$.

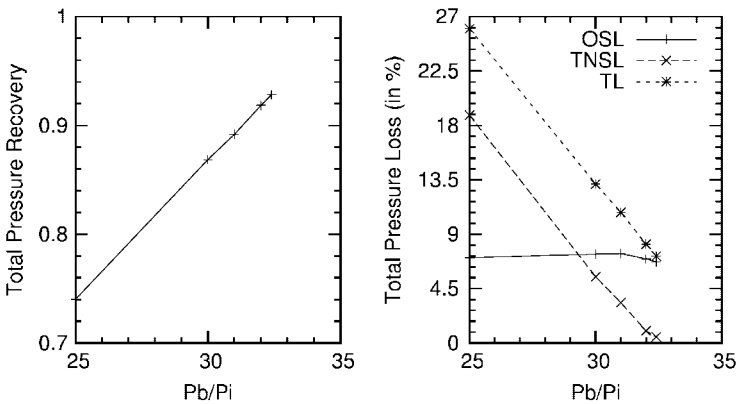

Figure 9. $M = 3$ flow in an air intake for the $R52.1$ ramp geometry: total pressure recovery (left) and the pressure loss due to oblique and normal shocks (right) for various values of the back pressure (OSL: losses due to oblique shocks, TNSL: loss due to terminal normal shock, and TL: total loss).

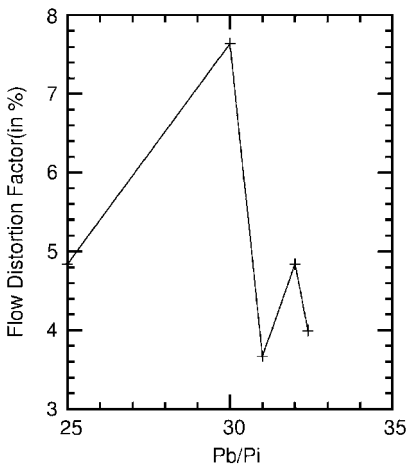

Figure 10. $M = 3$ flow in an air intake for the $R52.1$ ramp geometry: flow distortion index for various values of the back pressure.

4.5. *Effect of ramp geometry*

It is well known that in a quasi one-dimensional flow, for fixed inlet Mach number and exit pressure condition, the start-up of a intake solely depends on the throat-to-inlet capture area ratio (A_t/A_i). This fact has been widely accepted and practiced even for the case of two-dimensional flows. For example, to start an inlet it is suggested that either an increase in the throat area or momentarily over speeding, is required to establish the flow through a two-dimensional supersonic mixed-compression inlet. In the present study it is found that, in addition to A_t/A_i, the ramp geometry plays a significant role in the starting behaviour of the two-dimensional supersonic inlet. To demonstrate this phenomena, results are presented for

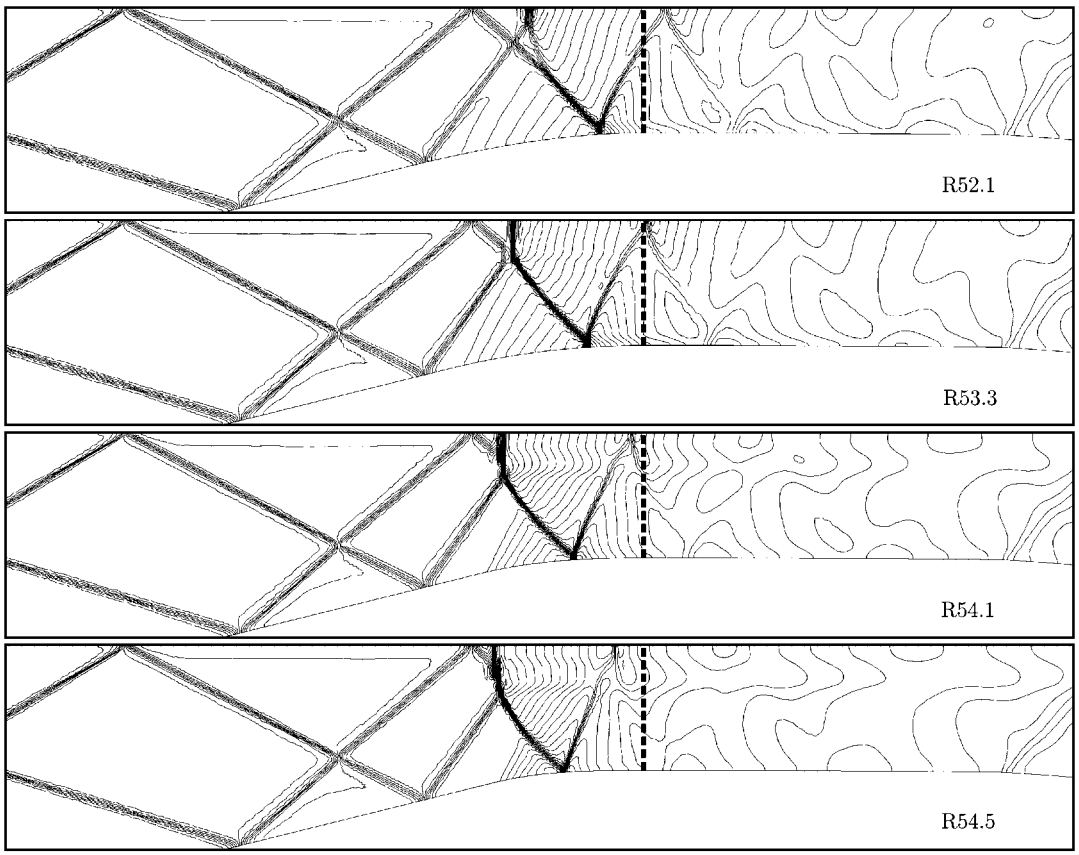

Figure 11. $M = 3$ flow in an air intake for various ramp geometries: Mach number distribution near the throat at $t = 0.8$. For all the cases the throat area is fixed and the conditions at the exit correspond to supersonic outflow. Also shown in broken lines is the location of throat.

an inlet for four different ramp geometries as shown in Figure 2. These are denoted by *R*54.5, *R*54.1, *R*53.3 and *R*52.1. The numerals reflect the end location of the second ramp, in inches, from the leading edge of the intake. The geometry of the inlet between the end of the second ramp and geometric throat is defined by a third-order polynomial. All the four geometries have the same throat area and its location. As seen from Figure 2, the increase in the second ramp length leads to higher curvature of the ramp just upstream of the throat.

Computations for all the four geometries correspond to supersonic outflow of the inlet; no boundary condition is imposed at the exit of the air intake. The finite element mesh used for the cases is very similar to that shown in Figure 3 and the same time step is utilized. All the other parameters for the four cases are identical. It is observed that the *R*54.5 and *R*54.1 inlets unstart, whereas the remaining two inlets start.

The instantaneous Mach number distribution for all the four cases at $t = 0.8$ is shown in Figure 11. Also shown in Figure 11 is the location of the geometric throat. It is observed

that the last main reflected oblique shock from the cowl surface lies in the convergent section for the $R54.5$ and $R54.1$ cases and in the divergent section for the other two geometries. The reflected oblique shock waves just upstream of the throat are associated with a normal shock segment close to the cowl surface. A study of the flow related to all the cases reveals that increase in the second ramp length leads to (a) stronger oblique shocks close to the throat and their more upstream location and (b) delay of the expansion waves to a more downstream location. These phenomena result in the formation of stronger normal shock segments at the cowl surface for the cases with longer second ramp. Consequently, the instantaneous mass flow rate at the throat reduces causing the flow to accumulate upstream of the throat. The mass flow rates, at $t = 0.8$, at the throat in the case of $R54.5$ and $R54.1$ are 99.76 and 99.92%, respectively, of the value based on the captured area. This causes the pressure in the inlet to rise and leads to the formation of a normal shock in the convergent portion. Subsequently, the inlet unstarts. In contrast, the mass flow rates at the throat, for $R52.1$ and $R53.3$, are equal to the value based on captured area. As is expected, inlet $R54.5$ takes lesser time than $R54.1$ to unstart.

These computations clearly indicate the significance of the geometry of the ramp in the throat region for 'starting' the inlet. It will be interesting to extend the study to investigate this effect on viscous flows.

5. CONCLUDING REMARKS

Finite element computation of inviscid flow in mixed compression two-dimensional supersonic inlets have been presented. The computations are capable of simulating the start-up and unstart of air intakes. The critical back pressure to inlet pressure ratio, beyond which the inlet unstarts, is found to be 32.4. Compared to experimental results and earlier computational results for viscous flows, as expected, it is found that the critical pressure and corresponding total pressure recovery are higher for inviscid flows. The variation between the total pressure recovery and the back pressure is almost linear. The location of the normal shock dictates the performance of a supersonic mixed compression inlet. Minimal losses occur when the normal shock is located close to the throat. However, the inlet unstarts as soon as the normal shock moves upstream of the throat in the convergent part of the intake. As the ratio of back pressure to inlet static pressure increases from 25 to 32.4, total pressure losses decrease from 26 to 7.21%. Distortion index is found in the acceptable range of 3–7%.

It is found that in addition to the throat-to-inlet capture area ratio, the ramp geometry plays an important role in the start-up dynamics. This finding may have significant implications in the design of air-intake systems and controlling their start-up.

NOMENCLATURE

ρ	density
$\mathbf{u}$	velocity with components (u_1, u_2)
e	total energy per unit mass
p	pressure
i	internal energy per unit mass

γ	ratio of specific heats
R	the ideal gas constant
θ	temperature
$\mathbf{U}$	vector of conservation variables $(\rho, \rho u_1, \rho u_2, \rho e)$
$\mathbf{F}_i$	Euler flux vector in direction i
$\mathbf{A}_i$	Euler Jacobian Matrix $(\partial \mathbf{F}_i / \partial \mathbf{U})$
$\mathscr{S}^h$	finite element trial function space
$\mathscr{V}^h$	weighting function space
n_{dof}	the number of degrees of freedom
$\mathbf{U}^h$	the discrete solution vector
$\mathbf{W}^h$	the weight function vector
c	the wave speed
h	the element length
δ	stabilizing coefficient in the shock-capturing term
$\boldsymbol{\tau}$	stabilizing coefficient in the SUPG terms
p_{b}	back-pressure at the exit of the intake
p_{i}	the inlet static pressure
p_0	stagnation pressure
TPR	total pressure recovery
ID	Inlet Distortion
OSL	pressure losses due to oblique shocks
TNSL	pressure loss due to terminal normal shock
TL	total pressure loss

REFERENCES

1. Hill PG, Peterson C. *Mechanics and Thermodynamics of Propulsion*. Addison-Wesley Publishing Company: Reading, MA, 1992.
2. Dailey CL. Supersonic diffuser instability. *Journal of the Aeronautical Sciences* 1955; **22**:733–749.
3. Anderson WE, Barth ND. Experimental investigation of a large-scale, two-dimensional, mixed-compression inlet system—performance at design conditions, $m_\infty = 3.0$. *Technical Report NASA TM X-2016*, NASA Ames Research Center, 1970.
4. Wasserbauer JF, Shaw RJ, Neumann HE. Design of a very-low-bleed mach 2.5 mixed-compression inlet with 45 percent internal contraction. *Technical Report NASA TM X-3135*, NASA, 1975.
5. Knight DD. Improved calculation of high speed inlet flows, part II: results. *AIAA Journal* 1981; **19**:172–179.
6. Knight DD. Calculation of simulated three-dimensional high speed inlet using the Navier–Stokes equations. *AIAA Paper 83-1165*, 1983.
7. Liang SM, Chan JJ. An improved upwind scheme for the Euler equations. *Journal of Computational Physics* 1989; **84**:461–473.
8. Liang SM, Chan JJ. Numerical investigation of supersonic mixed-compression inlet using an implicit upwind scheme. *Journal of Propulsion* 1992; **8**:158–167.
9. Gokhale SS, Kumar VR. Numerical computations of supersonic inlet flow. *International Journal for Numerical Methods in Fluids* 2001; **36**:597–617.
10. Hughes TJR, Brooks AN. A multi-dimensional upwind scheme with no crosswind diffusion. In *Finite Element Methods for Convection Dominated Flows*, Hughes TJR (ed.), AMD-Vol. 34. ASME: New York, 1979; 19–35.
11. Brooks AN, Hughes TJR. Streamline upwind/Petrov–Galerkin formulations for convection dominated flows with particular emphasis on the incompressible Navier–Stokes equations. *Computer Methods in Applied Mechanics and Engineering* 1982; **32**:199–259.
12. Tezduyar TE, Hughes TJR. Finite element formulations for convection dominated flows with particular emphasis on the compressible Euler equations. *Proceedings of AIAA 21st Aerospace Sciences Meeting*, *AIAA Paper 83-0125*, Reno, Nevada, 1983.

13. Le Beau GJ, Tezduyar TE. Finite element computation of compressible flows with the SUPG formulation. In *Advances in Finite Element Analysis in Fluid Dynamics*, Dhaubhadel MN, Engelman MS, Reddy JN (eds), FED-Vol. 123. ASME: New York, 1991; 21–27.
14. Mittal S. Finite element computation of unsteady viscous compressible flows. *Computer Methods in Applied Mechanics and Engineering* 1998; **157**:151–175.
15. Mittal S, Yadav S. Computation of flows in supersonic wind-tunnels. *Computer Methods in Applied Mechanics and Engineering* 2001; **191**:611–634.
16. Le Beau GJ. The finite element computation of compressible flows. *Master's Thesis*, Aerospace Engineering, University of Minnesota, 1990.
17. Hughes TJR, Tezduyar TE. Finite element methods for first-order hyperbolic systems with particular emphasis on the compressible Euler equations. *Computer Methods in Applied Mechanics and Engineering* 1984; **45**:217–284.
18. Hughes TJR, Mallet M, Mizukami A. A new finite element formulation for computational fluid dynamics: II. Beyond SUPG. *Computer Methods in Applied Mechanics and Engineering* 1986; **54**:341–355.
19. Hughes TJR. *The Finite Element Method. Linear Static and Dynamic Finite Element Analysis*. Prentice-Hall: Englewood Cliffs, NJ, 1987.
20. Mittal S. Finite element computation of unsteady viscous compressible flows past stationary airfoils. *Computational Mechanics* 1998; **21**:172–188.
21. Aliabadi SK, Tezduyar TE. Space–time finite element computation of compressible flows involving moving boundaries and interfaces. *Computer Methods in Applied Mechanics and Engineering* 1993; **107**(1–2): 209–224.
22. Hughes TJR, Mallet M. A new finite element formulation for computational fluid dynamics: IV. A discontinuity-capturing operator for multidimensional advective-diffusive systems. *Computer Methods in Applied Mechanics and Engineering* 1986; **58**:329–339.
23. Mittal S. Computation of internal and external compressible flows using EDICT. *International Journal of Computational Fluid Dynamics* 2001; **3**:225–241.

